

Lensing by galaxies in CNOC2 fields*

H. Hoekstra^{1,2,3}, M. Franx⁴, K. Kuijken³, R.G. Carlberg^{2,5}, H.K.C. Yee^{2,5}

¹ *CITA, University of Toronto, 60 St. George Street, Toronto, M5S 3H8, Canada*

² *Department of Astronomy, University of Toronto, 60 St. George Street, Toronto, M5S 3H8, Canada*

³ *Kapteyn Astronomical Institute, University of Groningen, Postbus 800, 9700 AV Groningen, The Netherlands*

⁴ *Leiden Observatory, P.O. Box 9513, 2300 RA Leiden, The Netherlands*

⁵ *Visiting Astronomer, Canada-France-Hawaii Telescope*

7 November 2018

ABSTRACT

We have observed two blank fields of approximately 30 by 23 arcminutes using the William Herschel Telescope. The fields have been studied as part of the Canadian Network for Observational Cosmology Field Galaxy Redshift Survey (CNOC2), and spectroscopic redshifts are available for 1125 galaxies in the two fields. We measured the lensing signal caused by large scale structure, and found that the result is consistent with current, more accurate measurements.

We study the galaxy-galaxy lensing signal of three overlapping samples of lenses (one with and two without redshift information), and detect a significant signal in all cases. The estimates for the velocity dispersion of an $L_B^*(z=0) = 5.6 \times 10^9 h^{-2} L_{B\odot}$ galaxy agree well for the various samples. The best fit singular isothermal sphere model to the ensemble averaged tangential distortion around the galaxies with redshifts yields a velocity dispersion of $\sigma_* = 130_{-17}^{+15}$ km/s, or a circular velocity of $V_c^* = 184_{-25}^{+22}$ km/s for an L_B^* galaxy, in good agreement with other studies.

We use a maximum likelihood analysis, where a parameterized mass model is compared to the data, to study the extent of galaxy dark matter halos. Making use of all available data, we find $\sigma_* = 111 \pm 12$ km/s (68.3% confidence, marginalised over the truncation parameter s) for a truncated isothermal sphere model in which all galaxies have the same mass-to-light ratio. The value of the truncation parameter s is not constrained that well, and we find $s_* = 260_{-73}^{+124} h^{-1}$ kpc (68.3% confidence, marginalised over σ_*), with a 99.7% confidence lower limit of $80 h^{-1}$ kpc. Interestingly, our results provide a 95% confidence upper limit of $556 h^{-1}$ kpc. The galaxy-galaxy lensing analysis allows us to estimate the average mass-to-light ratio of the field, which can be used to estimate Ω_m . The current result, however, depends strongly on the assumed scaling relation for s .

Subject headings: cosmology: observations – dark matter – gravitational lensing

1 INTRODUCTION

The (small) differential deflection of light rays by intervening structures allows us to study the projected mass distribution of the deflectors, without having to rely on assumptions about the state or nature of the deflecting matter. The first attempt to detect this effect, called weak gravitational lensing, was made by Tyson et al. (1984), who tried to measure the signal induced by an ensemble of galaxies. This area of astronomy blossomed with the successful measurements of the signal induced by rich clusters of galaxies at intermediate redshifts (e.g., Tyson, Wenk, & Valdes 1990; Bonnet, Mellier, & Fort 1994; Fahlman et al. 1994; Squires et al.

1996; Luppino & Kaiser 1997; Hoekstra et al. 1998; for an extensive review see Mellier 1999).

These studies of rich clusters were an important first step in demonstrating the feasibility of weak lensing analyses, but nowadays more and more studies concentrate on blank fields. For example, galaxy groups have masses intermediate between clusters of galaxies and galaxies. Hoekstra et al. (2001) measured the ensemble averaged weak lensing signal from a sample of 50 groups identified by Carlberg et al. (2001) in the Canadian Network for Observational Cosmology Field Galaxy Redshift Survey (CNOC2).

Other applications of wide field lensing are the measurement of the lensing signal caused by large scale structure (Bacon et al. 2000, 2002; Hoekstra et al. 2002a, 2002b; Kaiser, Wilson, & Luppino 2000; Refregier et al. 2002; van Waerbeke et al. 2000, 2001, 2002; Wittman et al. 2000), and the study of galaxy biasing (Hoekstra, Yee & Gladders 2001b; Hoekstra et al. 2002c). Another important applica-

* Based on observations made with the William Herschel Telescope operated on the island of La Palma by the Isaac Newton Group in the Spanish Observatorio del Roque de los Muchachos of the Instituto de Astrofísica de Canarias.

tion is the study of the dark matter halos of field galaxies (e.g., Brainerd, Blandford, & Smail 1996; Griffiths et al. 1996; Dell’Antonio & Tyson 1996; Hudson et al. 1998; Fischer et al. 2000; Wilson, Kaiser, & Luppino 2001; McKay et al. 2001; Smith et al. 2001).

Rotation curves of spiral galaxies have provided important evidence for the existence of dark matter halos (e.g., van Albada & Sancisi 1986). Also strong lensing studies of multiple imaged systems require massive halos to explain the observed image separations. However, both methods provide mainly constraints on the halo properties at relatively small radii. The weak lensing signal can be measured out to large projected distances, and in principle it can be a powerful probe of the potential at large radii, constraining the extent of the dark matter halos (e.g., Brainerd et al. 1996, Hudson et al. 1998; Fischer et al. 2000). Only satellite galaxies (e.g., Zaritsky & White 1994) provide another way to probe the outskirts of isolated galaxy halos.

The lensing signal induced by an individual galaxy is too low to be detected, and one has to study the ensemble averaged signal around a large number of lenses. Redshifts for the individual galaxies are useful, because they allow a proper scaling of the lensing signal around the galaxies, and they are necessary for studies of the evolution of the mass-to-light ratio of field galaxies from lensing. Hudson et al. (1998) were the first to make use of (photometric) redshifts in their galaxy-galaxy lensing analysis of the northern Hubble Deep Field. Unfortunately, the small area covered by the HDF limited the accuracy of their results.

The analysis of commissioning data of the Sloan Digital Sky Survey (SDSS) by Fischer et al. (2000) was a major step forward. Fischer et al. (2000) detected a very significant lensing signal, demonstrating the importance of the survey for the study of galaxy halos. More recently, McKay et al. (2001) used the available redshift information from the SDSS to study the galaxy-galaxy lensing signal as a function of galaxy properties.

We obtained deep R -band imaging data for two fields that have been studied as part of the CNOC2 Field Galaxy Redshift Survey (e.g., Yee et al. 2000). Earlier results on groups of galaxies, based on these data, were presented by Hoekstra et al. (2001a). In this paper, we use the data to study the galaxy-galaxy lensing signal of three overlapping samples of galaxies (one with, and two without redshift information).

The structure of the paper is as follows. In Section 2 we present the observations and data reduction. In this section we also describe in detail the object analysis and the corrections for the various observational distortions. In Section 3 we discuss the redshift distribution of the sources we use in this study. We investigate the lensing by large scale structure in Section 4. The analysis of the galaxy-galaxy lensing signal is presented in Section 5. In Section 6 we present our estimates of the field mass-to-light ratio for different halo models. Throughout the paper we take $H_0 = 100h$ km/s/Mpc, $\Omega_m = 0.2$, and $\Omega_\Lambda = 0$, although the results do not depend critically on the adopted cosmology.

field	RA	DEC	date
1447	14 ^h 47 ^m 04.3 ^s	09°12′39″	May 19 - 21 1998
2148	21 ^h 48 ^m 34 ^s	−05°56′00″	Aug 30 - Sep 2 1997

Table 1. Positions of the centres of the fields used for the weak lensing analysis. The last column gives the dates of the observations.

2 DATA

The Canadian Network for Observational Cosmology Field Galaxy Redshift Survey (CNOC2) targeted four widely separated patches on the sky to study the field population of galaxies in the universe. Redshifts of ~ 6200 galaxies with a nominal limit of $R_c = 21.5$ were measured, resulting in a large sample of galaxies at intermediate redshifts ($z = 0.12 - 0.55$). A detailed description of the survey, and the corresponding data reduction is given in Yee et al. (2000). In this paper we study the dark matter properties of the galaxies targeted by CNOC2, and to this end we make extensive use of the redshifts and multi-colour photometry obtained by the CNOC2 survey.

We observed the central parts of the two CNOC2 patches 1447+09 and 2148-05 (Yee et al. 2002, in preparation) using the 4.2m William Herschel Telescope (WHT) at La Palma. The images were taken using the prime focus camera, equipped with a thinned 2048×4096 pixels EEV10 chip, with a pixel scale of $0''.237$ pixel^{−1}. The resulting field of view of the camera is approximately $8'.1$ by $16'.2$.

The patches observed in the CNOC2 survey are much larger than the field of view of the WHT prime focus camera, and we observed a mosaic of 6 pointings. Table 1 lists the central positions of the observed fields as well as the dates of the observations. The typical integration time per pointing is one hour in R (see Table 2).

2.1 Data reduction

The images were flatfielded, using a master flatfield constructed from the science exposures. The images were calibrated using observations of standard stars from Landolt (1992).

The data for each pointing typically consists of 3 exposures of 1200s, which were taken with small offsets. Table 2 lists the total integration time, seeing, and number of detected objects for both observed fields. Note that because of adopted weighting scheme for the weak lensing analysis, the “effective” number of galaxies is approximately 30% of the total number. The data for the 1447 field have a median seeing of $\sim 0''.7$, whereas the data for the 2148 field are somewhat worse, with a seeing of $0''.85$.

The exposures had to be remapped before the images were combined into the final image, because of focal plane field distortions. We selected and measured the positions of stars in each of the exposures and used these as input for the IRAF tasks `geomap` and `geotran`. To obtain the final images that were used for the object analysis, the remapped images were simply averaged to ensure that neither cosmic ray rejection or medianing changed the shape of the PSF or the galaxies in a non-linear way.

Although a remapping of the images was necessary, the

field	t_{exp} [s]	seeing ["]	# objects	\bar{n} [arcmin ⁻²]	m_{lim} (90%)
(1)	(2)	(3)	(4)	(5)	(6)
1447-1	6000	0.75	5738	46	24.3
1447-2	3600	0.70	5545	44	24.5
1447-3	3600	0.65	6419	51	24.8
1447-4	3600	0.70	5570	45	24.6
1447-5	4800	0.70	6087	49	24.5
1447-6	3600	0.65	6826	55	24.8
2148-1	3600	1.0	4712	38	24.2
2148-2	3600	0.80	4976	40	24.3
2148-3	3600	0.75	5540	44	24.2
2148-4	4800	0.85	4804	38	24.2
2148-5	3600	0.90	4486	36	24.1
2148-6	3600	0.85	5110	41	24.2

Table 2. Summary of the deep WHT imaging. Column (1): identification of the pointing; (2) total integration time; (3) median seeing; (4) number of galaxies; (5) number density of galaxies; (6) 90% completeness limit in R .

camera induced distortion is small. The WHT prime focus observer’s manual lists the coefficients to estimate the telescope distortion, which is purely radial. We also calculated the distortion from a comparison of positions of bright stars that coincide with stars from the USNO catalog. The relatively large uncertainty ($\sim 0''.3$) in the astrometry of the USNO catalog limits the accuracy of this approach. The results, however, agree with the distortion derived from the parameters listed in the WHT observer’s manual, and we use the latter to calculate the camera distortion used in our analysis. We find that the induced shear is small: at most 0.66% in the corners of the field. The corrected weak lensing distortion field is obtained by subtracting the camera distortion from the observed distortions (which are corrected for PSF anisotropy), as described in Hoekstra et al. (1998).

2.2 Object detection and analysis

Our analysis technique is based on that developed by Kaiser, Squires, & Broadhurst (1995) and Luppino & Kaiser (1997), with a number of modifications which are described in Hoekstra et al. (1998). We analyse each pointing separately as the seeing and PSF anisotropy vary between each exposure. After the catalogs have been corrected for the various observational effects, they are combined into a master catalog which covers the complete field that is observed.

The first step in the analysis is to detect the faint galaxy images, for which we used the hierarchical peak finding algorithm from Kaiser et al. (1995). The peak finder also provides an estimate for the Gaussian scale length r_g of the object. We select objects which were detected with a significance $\nu > 5\sigma$ over the local sky in the combined images. This galaxies are used for the weak lensing analysis. We also run the peak finder on the images of the single exposures. We do a coincidence test on these catalogs and classify extremely small, but very significant objects as cosmic rays, which are removed from the catalog that is used for the object analysis.

Some faint cosmic rays may hit galaxies, and conse-

quently might not be recognized as cosmic rays. Based on the number of cosmic ray hits, and the area covered by galaxies we find that less than 0.2% of the galaxies might be affected. Also, cosmic rays only introduce additional noise in the shape measurement, but do not bias the result. Consequently we conclude that remaining cosmic rays have a negligible effect on our results.

For the weak lensing analysis we select objects which are detected in at least two of the shorter exposures. The objects which are detected in only one of the shorter exposures are small faint objects, which are not useful as their shape parameters are noisy. The resulting catalogs are inspected visually in order to remove spurious detections, such as spikes from saturated stars, HII regions in resolved galaxies, etc.

For all detected objects we measure the apparent magnitude in an aperture with a radius of 3 times the Gaussian scale length of the object, the half light radius, and the shape parameters (polarization and polarizabilities). We also estimate the error on the polarization following Hoekstra, Franx, & Kuijken (2000).

2.3 PSF correction

To measure the small, lensing induced, distortions in the images of the faint galaxies it is important to correct the shapes for observational effects, such as PSF anisotropy and seeing: PSF anisotropy can mimic a lensing signal, and the correction for seeing is required to relate the measured shapes to the real lensing signal.

To do so, we follow the procedure outlined in Hoekstra et al. (1998) (which is based on Kaiser et al. 1995; Luppino & Kaiser 1997). We select a sample of moderately bright stars from our observations. These are used to characterize the PSF anisotropy and seeing. Figure 1 shows a typical result for one of the pointings. We fit a second order polynomial to the observed shape parameters of the stars, and this model is used to correct for the PSF anisotropy. Figure 1b also shows the residual polarization of the stars after the correction. The residuals are small indicating that we can reliably correct for the PSF anisotropy.

The next step is to correct the shapes for the circularization by the PSF. The stars that were used to study the PSF anisotropy are also used to compute the ‘pre-seeing’ shear polarizability P^γ (Luppino & Kaiser 1997; Hoekstra et al. 1998). The measurement of P^γ is very noisy, and we combine the estimates of many galaxies to reduce the noise. We also found that the size of the PSF, and thus the correction, depends on the position on the chip. The variation, however, is small: about 10% maximum. To account for this, we bin the raw polarizabilities not only in bins of r_g , but also as a function of position. For a given r_g we fit a second order polynomial to the median P^γ ’s as a function of position, and use the results to compute the P^γ for each galaxy. Figure 2a shows P^γ as a function of r_g .

Objects with small values for P^γ require large corrections, thus increasing the noise. The weighting scheme suggested in Hoekstra et al. (2000) gives already less weight to these objects, but in addition we exclude objects with $P^\gamma \leq 0.1$

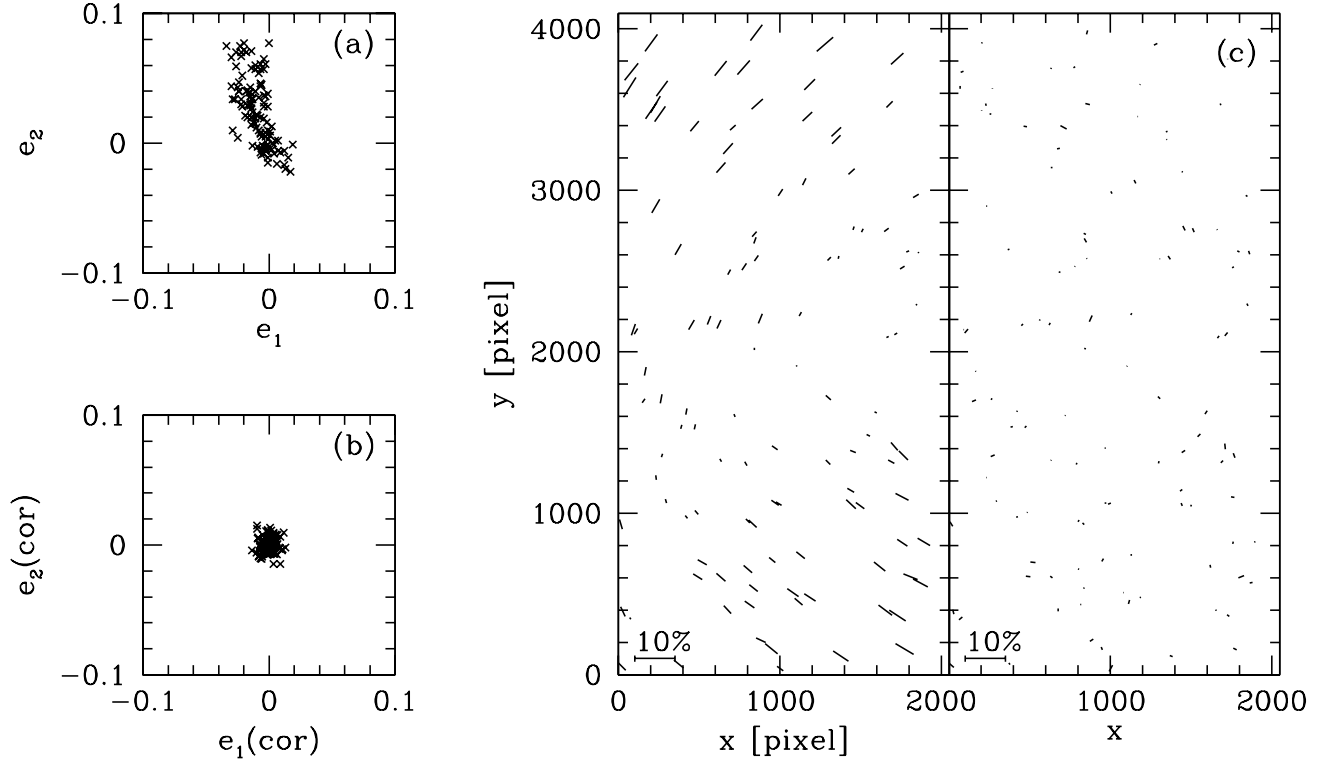


Figure 1. Shape of the PSF in one of the pointings of the 1447 field; (a) the polarizations of the stars before correction; (b) residual polarization after correcting for the PSF anisotropy using a second order polynomial fit to the data. (c) PSF anisotropy as a function of position on the chip. The left panel shows the PSF anisotropy before correction. To show the higher order components the average polarization has been subtracted. The direction of the sticks indicates the major axis of the PSF, whereas the length corresponds to the size of the anisotropy. The right panel shows the residuals in the stellar polarizations after correction.

3 REDSHIFTS OF LENSES AND SOURCES

For a given mass distribution, the amplitude of the weak lensing signal is proportional to the dimensionless mass surface density

$$\kappa(\vec{x}) = \frac{\Sigma(\vec{x})}{\Sigma_{\text{crit}}}, \quad (1)$$

where the critical surface density is defined as

$$\Sigma_{\text{crit}} = \frac{c^2}{4\pi G} \frac{D_s}{D_1 D_{1s}} = \frac{c^2}{4\pi G D_1 \beta}. \quad (2)$$

Here D_s , D_1 , and D_{1s} correspond to the angular diameter distances between the observer and the source, observer and the lens, and the lens and the source. The lensing signal depends on both the redshifts of the lenses and the sources, and the dependence on the source redshift is characterized by β , which is defined as

$$\beta = \max[0, D_{1s}/D_s]. \quad (3)$$

If the redshift of the lens approaches that of the source, the amplitude of the lensing signal, which is proportional to β , decreases.

Most of the lensing signal comes from galaxies that are generally too faint to be included in redshift surveys. To re-

late the lensing signal to a physical mass it is necessary to know the redshift distribution of the faint background galaxies. To this end, we use photometric redshift distributions from the Hubble Deep Fields North and South (Fernández-Soto, Lanzetta, & Yahil 1999). Hoekstra et al. (2000) used these results for their analysis of the distant cluster MS 1054-03 ($z = 0.83$), and concluded that these redshift distributions provide a good approximation of the true distribution. We use the colours of the galaxies in the HDFs to derive their R band magnitude. For each lens-source pair we compute the corresponding value of β .

The lenses considered in our analysis are at much lower redshifts than MS 1054-03, and consequently the uncertainty in the value of β is small. Based on field-to-field variation in the redshift distribution and the uncertainty due to the finite number of galaxies in the Hubble Deep Fields, we estimate that the uncertainty in β is 2%.

4 LENSING BY LARGE SCALE STRUCTURE

One of the selection criteria for the CNOC2 fields (which are described in Yee et al. 2000) is that no known nearby rich cluster should be in the field. However, the observed fields

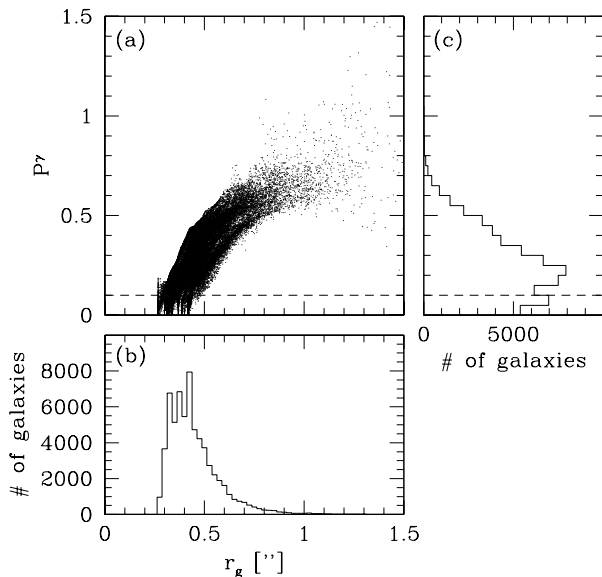


Figure 2. (a) P^γ as a function of r_g for all galaxies. Due to seeing variations the curves for the various fields blend; (b) number of galaxies with a given r_g ; (c) number of galaxies with a given value of P^γ . For the weak lensing analysis we restrict the sample to galaxies with $P^\gamma \geq 0.1$.

might contain distant massive clusters. In principle, such clusters can be found in a weak lensing analysis, provided they are massive enough (e.g., Wittman et al. 2001), even if they are “dark” (see Erben et al. 2000). We note that projection effects can actually introduce spurious detections (e.g., Hoekstra 2001; White, van Waerbeke & Mackey 2002).

To investigate possible structures in the CNOC2 fields, we reconstructed maps of the dimensionless surface density, using the original Kaiser & Squires (1993) algorithm. The resulting mass maps are consistent with noise maps. We find a few 3σ peaks, but no obvious counterparts are seen in the number counts of bright galaxies. The mass maps have been smoothed with a Gaussian with a FWHM of 1 arcminute, resulting in approximately 500 independent points in each map. Therefore one expects about three 3σ peaks.

It is useful to estimate the mass detection limit for our data. We assume that the cluster mass profile is well described by a singular isothermal sphere (SIS):

$$\kappa = \frac{r_E}{2r}, \quad (4)$$

where r_E is the Einstein radius. The observed scatter in the shapes of the sources results in a typical uncertainty in the Einstein radius r_E of $\sim 2''$. We fit SIS models out to 5 arcminutes, but note that the uncertainty in the determination of the Einstein radius does not depend significantly on this particular range. Hence, we should be able to detect a cluster with $r_E > 6''$ (at the 3σ level). The velocity dispersion of the SIS model is given in km/s by

$$\sigma = 186.3 \sqrt{\frac{r_E}{\beta}} \text{ km/s}, \quad (5)$$

when r_E is given in arcseconds. Given the redshift distribu-

field	$\langle g_1 \rangle$	$\langle g_2 \rangle$	σ_g
1447	-0.00334	0.00144	0.00226
2148	0.00323	-0.00140	0.00254

Table 3. Average distortion in the observed fields. The errors in the measurements are given in the last column. The values are small, which suggest that the correction for the PSF anisotropy has worked well.

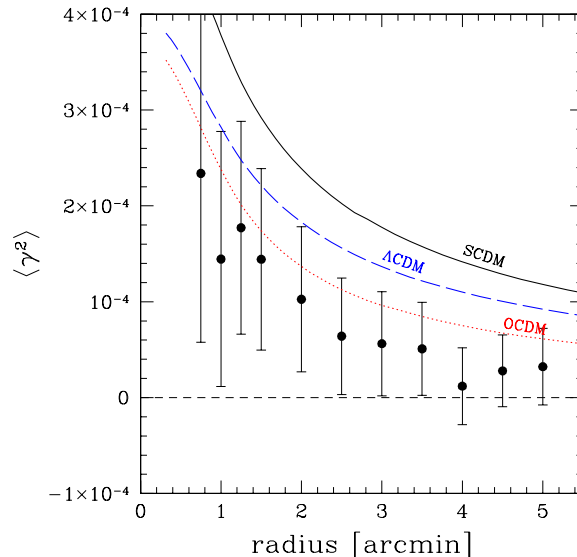


Figure 3. The observed variance of $\langle \gamma^2 \rangle$ as a function of the radius of the aperture in which the shear is averaged. Note that the points are correlated. The error bars do not include the additional uncertainty caused by cosmic variance. For reference we have displayed the expected variances for three different cosmologies: SCDM ($\Omega_m = 1.0$; $\Omega_\Lambda = 0$; $\Gamma = 0.5$; $\sigma_8 = 0.5$), OCDM ($\Omega_m = 0.3$; $\Omega_\Lambda = 0$; $\Gamma = 0.21$; $\sigma_8 = 0.85$), and LCDM ($\Omega_m = 0.3$; $\Omega_\Lambda = 0.7$; $\Gamma = 0.21$; $\sigma_8 = 0.9$).

tion of our sources a cluster with a velocity dispersion of 630 km/s at $z = 0.2$ would be detectable, whereas a cluster at $z = 0.5$ would have to have a velocity dispersion larger than 900 km/s. Such rich clusters would have been detected in the CNOC2 redshift survey. A detectable cluster at $z > 0.5$ would have to be even more massive. Such massive systems are very rare, and are unlikely to be in the observed fields. Based on the mass reconstructions we find no massive clusters in the CNOC2 fields.

Although we do not detect significant structures in the CNOC2 field, any large scale structure along the line of sight will introduce an excess alignment in the shapes of the faint galaxies (compared to a random field). The measurement of this signal provides a direct measurement of the statistical properties of the large scale mass distribution (e.g., Blandford et al 1991; Kaiser 1992; Bernardeau, van Waerbeke, & Mellier 1997; Schneider et al. 1998).

A widely used method is to look for the excess variance in an aperture: the top-hat variance. This measurement as a function of scale can be compared to predictions from cos-

mological models. The measurement is difficult, and residual systematics (such as an imperfect correction for PSF anisotropy) increase the observed variance.

Since the first detections (Bacon et al. 2000; Kaiser, Wilson, & Luppino 2000; Maoli et al. 2001; van Waerbeke et al. 2000; Wittman et al. 2000) tremendous progress has been made. The most recent results are based on large data sets, and yield consistent results, despite the small statistical errors (e.g., Bacon et al. 2002; Hoekstra et al. 2002a, 2002b; Refregier et al. 2002; van Waerbeke et al. 2001, 2002). The area covered by the two CNOC2 fields is smaller than the area covered by these studies, but it is still interesting to examine our results and compare them to the predictions: although the analysis will not provide tight constraints on the cosmology, it is a useful test whether residual systematics are present in the data.

For the analysis, we use galaxies with apparent magnitudes $21 < R < 26$ as our sample of sources. The measurements of the average distortion of the two fields are presented in Table 3. To measure the excess top-hat variance as a function of aperture radius, we tile the observed fields with apertures of a given scale, compute the variance, and subtract the contribution from the intrinsic shapes of the galaxies (e.g., Bacon et al. 2000; Kaiser et al. 2000; Hoekstra et al. 2002a; van Waerbeke et al. 2000, 2001).

The results are presented in Figure 3. The error only includes the statistical uncertainty caused by the intrinsic shapes of the sources, and does not include the contribution from cosmic variance. Also note that the points are correlated. The measured variances are small, and consistent with current, more accurate measurements.

The top-hat variance is very sensitive to residual PSF anisotropy, and can be used to test the accuracy of the correction. For instance, if we do not correct the shapes of the galaxies for PSF anisotropy, we measure an excess variance $\langle \gamma^2 \rangle = (8.4 \pm 0.6) \times 10^{-3}$ at a scale of 1 arcminute, 60 times larger than the signal presented in Figure 3. If we subtract 90% (under-correction) or 110% (over-correction) of the PSF anisotropy, the observed variance increases by a factor ~ 2 . Because any residual PSF anisotropy will increase the signal, this test indicates that the adopted correction yields the minimum (or close to) variance.

5 GALAXY-GALAXY LENSING

We use two different methods to study the lensing signal caused by the field galaxies. First we measure the ensemble averaged tangential distortion around the lens galaxies (galaxy-mass correlation function), which provides a robust estimate of the lensing signal. We also perform a maximum likelihood analysis, which is described in Section 5.3.

It is important to note that the measurement of the galaxy-galaxy lensing signal is much less sensitive to a small residual systematics: we measure the lensing signal that is perpendicular to the line connecting many lens-source pairs. These connecting lines are randomly oriented with respect to the PSF anisotropy, and hence suppress any residual systematics. Given the results obtained for the top-hat smoothed variance (see Section 4), we expect that the effect of residual systematics is negligible.

In Table 4 we present the three subsamples of lenses

that we study. The ‘faint’ and the ‘bright’ sample are magnitude limited, and we use statistical redshift distributions for the lenses to infer the average halo properties. The ‘CNOC2’ sample has the same magnitude limits as the ‘bright’ sample, but consists only of galaxies with spectroscopic redshifts. It includes approximately half of the galaxies of the ‘bright’ sample. The ‘faint’ sample is comparable to the sample of lenses studied by Brainerd et al. (1996) who used $20 < r_{\text{lens}} < 23$, and $23 < r_{\text{source}} < 24$. Brainerd et al. (1996) did not use fainter sources, because they did not correct for observational distortions.

5.1 Lenses selected irrespective of redshift information

The ensemble averaged tangential distortion as a function of radius from the lens is a well established way to present the galaxy-galaxy lensing signal (e.g., Brainerd et al. 1996; Hudson et al. 1998; Fischer et al. 2000; McKay et al. 2001). The results for the ‘faint’ and the ‘bright’ sample are shown in Figure 4. For both samples a significant lensing signal is detected. If the measured signal is caused by gravitational lensing, no signal should be observed when the sources are rotated by $\pi/4$. The results of this test are shown in figure 4b and d, and no signal is seen indeed.

If the lenses are distributed randomly on the sky, the tangential distortion profile can be related directly to the ensemble averaged mass profile of the lenses. In reality the lenses cluster, and the observed signal is the convolution of the mass profile and the galaxy correlation function: the tangential shear profile measures the galaxy-mass cross-correlation function. As a result mass estimates based on the tangential shear profile are biased high, because at large distances from the lens, one measures the mass of the lens and associated galaxies. However, the lens dominates the signal on small scales.

We fit a SIS model to the tangential distortion profiles presented in figure 4. We do not know the redshifts of the individual lenses in these samples, and consequently we can only determine the ensemble averaged Einstein radius $\langle r_E \rangle$. For the ‘faint’ sample we find a best fit Einstein radius $\langle r_E \rangle = 0''.118 \pm 0''.025$, and for the ‘bright’ sample we obtain $\langle r_E \rangle = 0''.176 \pm 0''.045$.

We examined the effect of an imperfect correction for PSF anisotropy on the determination of the Einstein radius. Even in the extreme case that no correction is applied the derived value is changed by only 5%. In the case of a 90% or 110% correction of the PSF anisotropy, the signal is changed by $\sim 1\%$. Based on the results obtained for the top-hat smoothed variance (see Section 4), we conclude that the effect of an imperfect correction of the PSF anisotropy is much smaller than 1%, and hence is negligible.

We use the effective β for these samples (see column 6 of Table 4) to derive a mass weighted average velocity dispersion $\langle \sigma^2 \rangle^{1/2} = 108_{-12}^{+11}$ km/s for the ‘faint’ sample, and $\langle \sigma^2 \rangle^{1/2} = 122_{-17}^{+15}$ km/s for the ‘bright’ sample. The corresponding circular velocity can be calculated using $V_c = \sqrt{2}\sigma$.

The derived values of $\langle \sigma^2 \rangle^{1/2}$ depend on the selection of the sample of lens galaxies, and one cannot compare these results to findings of other studies, given the differences in

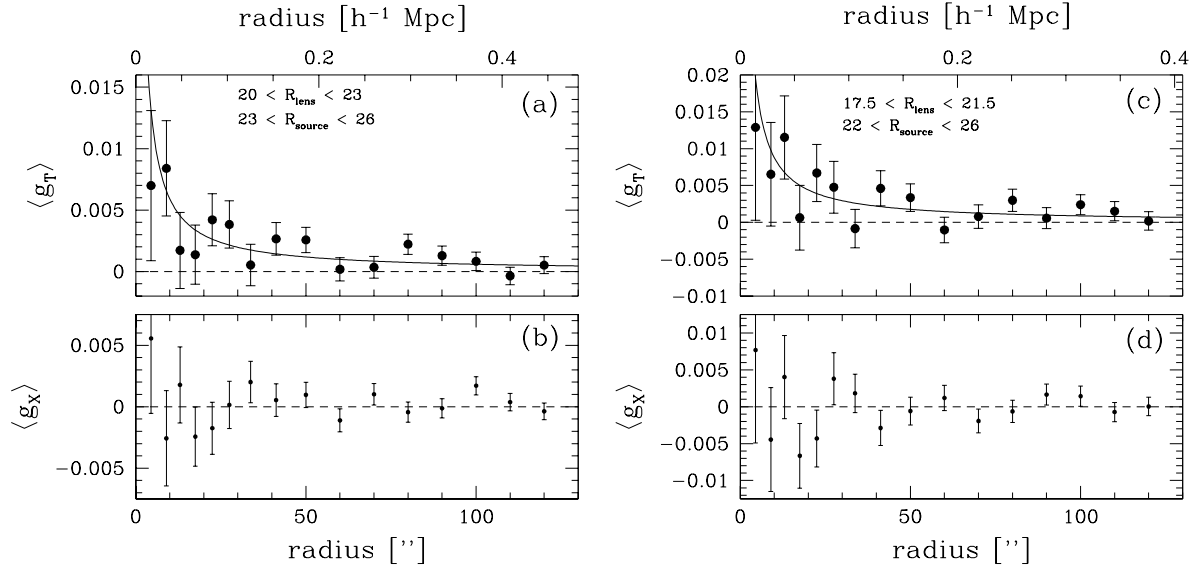


Figure 4. (a) The ensemble averaged tangential distortion for the ‘faint’ sample. The solid line corresponds to the best SIS model fit, which has $r_E = 0''.118 \pm 0''.025$. Panel c shows the signal around the ‘bright’ sample, and we find $r_E = 0''.176 \pm 0''.045$. Panels b and d show the average signal when the sources are rotated by $\pi/4$. No signal should be present if the signal in panels a and c is caused by lensing.

(1) sample	(2) lens	(3) source	(4) # lens	(5) z_{lens}	(6) $\langle \beta \rangle$	(7) $\langle r_E \rangle$ [']	(8) $\langle r_E^* \rangle$ [']	(9) σ_* [km/s]	(10) V_c^* [km/s]	(11) σ_* [km/s]
faint	$20 < R < 23$	$23 < R < 26$	8715	0.46	0.35 ± 0.01	0.118 ± 0.026	0.159 ± 0.035	126^{+13}_{-15}	178^{+19}_{-21}	124^{+13}_{-15}
bright	$17.5 < R < 21.5$	$22 < R < 26$	2125	0.34	0.41 ± 0.01	0.176 ± 0.046	0.161 ± 0.042	117^{+15}_{-17}	165^{+21}_{-23}	115^{+15}_{-17}
CNOC2	$17.5 < R < 21.5$	$22 < R < 26$	1125	0.36	0.40 ± 0.01	0.196 ± 0.047	0.196 ± 0.048	130^{+15}_{-17}	184^{+22}_{-25}	129^{+15}_{-17}

Table 4. Properties and results for the different samples of lens galaxies. (2) the range in apparent magnitude of the lens galaxies; (3) range in apparent magnitude for the sources; (4) number of lens galaxies; (5) median redshift of the lenses; (6) average value of β based on the redshift distributions of the lenses and the sources. (7) best fit Einstein radius; (8) estimate for the Einstein radius of an L_B^* galaxy; (9) best estimate for the velocity dispersion of an L_B^* galaxy under the assumption that the luminosity evolves $\propto (1+z)$; (10) corresponding circular velocity; (11) the velocity dispersion of an L_B^* galaxy for no luminosity evolution.

sample selection. Instead we estimate the velocity dispersion (or circular velocity) of an L_B^* galaxy. We assume a scaling relation between the velocity dispersion and the luminosity of the galaxy of the form

$$\sigma \propto L_B^{1/4}, \text{ or } V_c \propto L_B^{1/4}. \quad (6)$$

We also assume that the luminosity of a lens of given mass evolves with redshift $\propto (1+z)$ (e.g., Lin et al. 1999). With these assumptions the average value of the Einstein radius (in radians) is given by

$$\langle r_E \rangle = \frac{4\pi}{c^2} \frac{\sigma_*^2}{\sqrt{L_B^*(z=0)}} \left\langle \beta \sqrt{\frac{L_B^{\text{obs}}}{1+z}} \right\rangle, \quad (7)$$

where L_B^{obs} is the observed intrinsic luminosity of the galaxy. We also introduce $\langle r_E^* \rangle$

$$\langle r_E^* \rangle = \frac{4\pi}{c^2} \sigma_*^2 \langle \beta \rangle, \quad (8)$$

which is the Einstein radius of an L_B^* galaxy at the average redshift of the sample of lenses.

The redshift distributions of the sources and the ‘faint’ lens sample are derived from the photometric redshift distributions of the HDF North and South ((Fernández-Soto, Lanzetta, & Yahil 1999). For the ‘bright’ sample we use the redshift distribution from the CNOC2 survey with the proper weighting to take into account the incompleteness of the survey. To determine the restframe B luminosities we use template spectra for a range in spectral types and compute the corresponding passband corrections as a function of redshift and galaxy colour (this procedure is similar to the one described in van Dokkum & Franx 1996).

Lin et al. (1999) have studied the field galaxy luminosity function at intermediate redshift from the CNOC2 survey, and derived $M_B^*(z=0.3) = -19.18 + 5 \log h$, which corresponds to a luminosity of $7.3 \times 10^9 h^{-2} L_{B\odot}$. With our assumed luminosity evolution, this results in $L_B^*(z=0) = 5.6 \times 10^9 h^{-2} L_{B\odot}$. Madgwick et al. (2002) derived

$M_B^* = -19.55 + 5 \log h$ from the the 2dF redshift survey, which probes lower redshifts. Hence, the CNOC2 value (Lin et al. 1999) is rather low, in particular with our choice of luminosity evolution. Throughout the paper we assume that the luminosity evolves $\propto (1+z)$, but for reference we also list the results for the no-evolution scenario, in which case $L_B^*(z=0) = 7.3 \times 10^9 h^{-2} L_{B\odot}$.

Column 8 in Table 4 lists the derived Einstein radii of an L_B^* galaxy for the ‘bright’ and the ‘faint’ sample. For the ‘bright’ sample the observed $\langle r_E \rangle$ is actually very close to r_E^* . For the ‘faint’ sample we find that the observed $\langle r_E \rangle = 0.74 \langle r_E^* \rangle$. Columns 9 and 10 list the velocity dispersion and circular velocity of an L_B^* galaxy under the assumption that the luminosity evolves $\propto (1+z)$. Column 11 shows the resulting velocity dispersion without luminosity evolution. Coincidentally, the values for σ_* for the evolving and non-evolving case are very similar. Furthermore, the results for the faint and bright sample agree well with one another.

5.2 Lenses with redshifts from CNOC2

Redshifts for the lens galaxies are useful because they allow a proper scaling of the signals around the lens galaxies. Intrinsically faint (and therefore low mass) galaxies, or galaxies with redshifts comparable to the source galaxies are given lower weights. We scale the observed distortion of each galaxy, as well as its error, such that it corresponds to that of an L_B^* galaxy at the median redshift of the ‘CNOC2’ sample

$$g_T^{\text{scale}} = \left(\frac{5.6 \times 10^9 (1+z)}{L_B} \right)^{1/2} \left(\frac{0.4}{\beta} \right) g_T^{\text{obs}}, \quad (9)$$

where we assumed that the luminosity scales with the fourth power of the velocity dispersion. The value of β is calculated for each galaxy separately, based on its redshift, and the redshift distribution of the sources. The sample of lenses consists of 1125 galaxies with spectroscopic redshifts, and $17.5 < R_{\text{lens}} < 21.5$. We note that, because of the selection of these galaxies, the sampling in apparent magnitude is not uniform (the completeness for the fainter galaxies is lower). Figure 5a shows the resulting average tangential distortion as a function of radius around an L_B^* galaxy at $z = 0.36$. A significant galaxy-galaxy lensing signal is detected.

The best fit SIS model to the scaled tangential distortion yields an Einstein radius $r_E = 0''.196 \pm 0''.047$. From this result we derive an average velocity dispersion of $\sigma = 130_{-17}^{+15}$ km/s or circular velocity of $V_c = 184_{-25}^{+22}$ km/s for an L_B^* galaxy. If we assume no luminosity evolution, we obtain $\sigma_* = 129_{-17}^{+15}$ km/s (with $L_B^*(z=0) = 7.3 \times 10^9 h^{-2} L_{B\odot}$).

The number of lenses in the ‘CNOC2’ sample is half that of the ‘bright’ sample, but the signal-to-noise ratio with which the lensing signal is detected is similar. Thus redshifts for the lenses are useful as they can be used to improve the signal-to-noise ratio of the measurement. A comparison of the results for the different samples (which are listed in Table 4) shows a good agreement.

We note that we have made assumptions about the luminosity evolution and the scaling relations. The redshift information for the lenses is crucial when one would like to constrain the scaling relations or study the evolution of the mass-to-light ratio of these field galaxies.

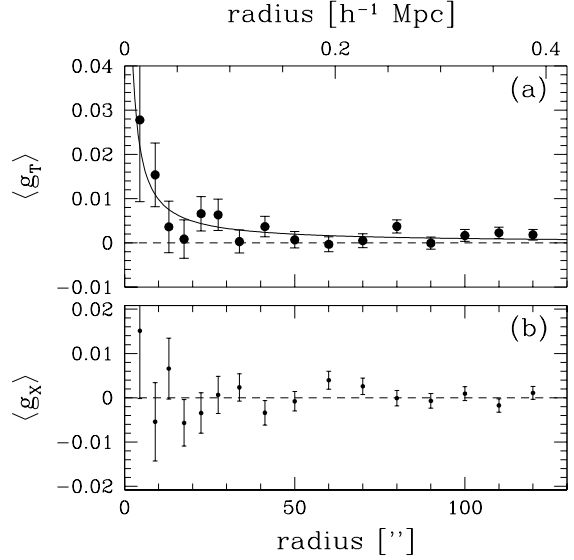


Figure 5. (a) The ensemble averaged tangential distortion around galaxies with $17.5 < R < 21.5$ and measured spectroscopic redshifts, scaled to an L_B^* galaxy at a redshift $z = 0.36$. The solid line corresponds to the best SIS model fit, which has $r_E = 0''.196 \pm 0''.047$. (b) The average signal when the sources are rotated by $\pi/4$. No signal should be present if the signal in panel a is caused by lensing.

5.3 Sizes of galaxy halos

As mentioned above, the clustering of lenses will bias the mass estimates inferred from the observed tangential distortion profile. In this section we use a parameterised model for the mass distribution of individual galaxies and compare the predicted distortions to the observed distortion field. We use a truncated halo model, in order to constrain both the mass and the extent of the dark matter halos.

This approach naturally takes into account the clustering of the lenses in the sample. Furthermore, we make use of both components of the distortion. It is important to note that the contribution of associated faint galaxies is not accounted for. The effect of a large-scale cosmological shear on the parameter estimation is negligible because one measures the lensing signal for many randomly oriented lens-source pairs. The effect of clusters/groups on the results is examined in Section 5.4.

A useful model to describe a truncated halo is (Schneider & Rix 1997)

$$\Sigma(r) = \frac{\sigma^2}{2Gr} \left(1 - \frac{r}{\sqrt{r^2 + s^2}} \right), \quad (10)$$

where s is a measure of the truncation radius. The total mass of this model is finite, and half of the mass is contained within $r = \frac{3}{4}s$. The total mass is given by

$$M_{\text{tot}} = \frac{\pi \sigma^2}{G} s = 7.3 \times 10^{12} \left(\frac{\sigma}{100 \text{ km/s}} \right)^2 \left(\frac{s}{1 \text{ Mpc}} \right). \quad (11)$$

The scatter in the polarizations of the galaxies is approximately constant with apparent magnitude, and it can be well approximated by a Gaussian distribution. In that

case the log-likelihood follows a χ^2 distribution with the number of degrees of freedom equal to the number of free model parameters (e.g., Hudson et al. 1998), and the determination of confidence intervals is straightforward. The log-likelihood is given by the sum over the two components of the polarization e_i of all the source galaxies

$$\log \mathcal{L} = - \sum_{i,j} \left(\frac{e_{i,j} - g_{i,j}(\sigma_*, s_*) P_j^\gamma}{\sigma_{e_j}} \right)^2, \quad (12)$$

where $g_{i,j}$ are the model distortions, P_j^γ is the shear polarizability, $e_{i,j}$ are the image polarizations for the j th galaxy, and σ_{e_j} is the uncertainty in the shape measurement of the j th galaxy.

In our maximum likelihood analysis we ignore the contribution from lenses outside the field of view (e.g., Hudson et al. 1998). For small fields of view this tends to lower the resulting σ_* and s_* somewhat. The area covered by our observations is much larger than the HDF North studied by Hudson et al. (1998), and we find that the effect on our estimates of σ_* and s_* is negligible.

To scale the signals of the various lenses we use again $\sigma \propto L_B^{1/4}$, which is based on both dynamical and observational considerations. The situation is different for the truncation parameter s , because there are no observational constraints. Here we will explore several cases.

If all halos have the same value for s the total mass-to-light ratio scales as $(M/L)_{\text{tot}} \propto L^{-1/2}$ (where we assume that $L \propto \sigma^4$). Thus the mass-to-light ratios of more luminous galaxies are lower. Another option is to take $(M/L)_{\text{tot}} = \text{constant}$ for all galaxies. This choice is equivalent to taking $s \propto \sigma^2$ (e.g., Brainerd et al. 1996; Hudson et al. 1998). The last relation we examine is $s \propto \sigma^4$, which gives $(M/L)_{\text{tot}} \propto L^{1/2}$.

Figure 6 shows the results for the ‘CNOC2’ sample, for which the individual redshifts of the lenses are known. It shows the likelihood contours for the parameters σ_* and s_* jointly. The result for a constant s for all galaxies is presented in figure 6a, and the result for $s \propto \sigma^2$ is shown in figure 6b. We omit the likelihood plot $s \propto \sigma^4$, but we list the best fit parameters (68.3% confidence limits) for all three models in Table 5a. The results change slightly when we assume no luminosity evolution, and the values of the parameters are listed in Table 5d. The confidence intervals on σ_* (s_*) listed in Tables 5a and d are obtained by marginalising over s_* (σ_*). Note that these confidence intervals cannot be inferred directly from Figure 6 (e.g., Press et al. 1992, Numerical Recipes in C, Figure 15.6.3).

We also examined the influence of an imperfect correction for PSF anisotropy. The change in the derived velocity dispersion is approximately 1% if we under or overcorrect by 10%. The value of s_* is changed by $\sim 6\%$ in these cases. As we have demonstrated above, the actual correction for PSF anisotropy is much better than 10%, and hence we find it to be negligible.

In all cases the velocity dispersion is well constrained, and in good agreement with the results from the ensemble averaged tangential distortion. The value of the truncation parameter has significant freedom, and the value of s_* depends strongly on the assumed scaling relation. We find that the value of s_* decreases when s scales with a high power of the velocity dispersion. The minimum χ^2 for the three mod-

els are comparable, and no scaling relation for s is preferred over the other ones. Table 5a also lists the best estimate and the 68.3% confidence limits for the total mass and mass-to-light ratio of an L_B^0 galaxy. The total galaxy mass is not well constrained, mainly because of the large uncertainty in the value of the truncation parameter s_* .

The mass model uses only half of the galaxies with $17.5 < R < 21.5$, and therefore it ignores the contributions of the other galaxies (they are given zero mass). If the remaining galaxies were distributed randomly, their contribution to the lensing signal is that of noise. We know, however, that galaxies are clustered. Consequently the mass model will associate the mass of the galaxies without redshifts with the galaxies in the ‘CNOC2’ sample that have measured redshifts.

To examine this in more detail we study the ‘bright’ sample, which is selected irrespective of redshift information. Even this selection is not ideal, neighbouring galaxies that are fainter than the applied magnitude limits are still excluded. If a substantial fraction of the mass is in these galaxies both the values of σ_* and s_* are overestimated.

Figure 7 shows the resulting likelihood contours. To obtain figure 7 we have assumed that all halos have the same velocity dispersion, and the same value for s in arcseconds. We find $\langle \sigma^2 \rangle^{1/2} = 117_{-15}^{+13}$ km/s, and $\langle s \rangle = 88_{-27}^{+43}$ arcseconds (68.3% confidence). At the average redshift of the lenses, this corresponds to $\langle s \rangle = 284_{-87}^{+139}$ h^{-1} kpc. The estimate for $\langle s \rangle$ is a weighted average over the value of s for all the galaxies, which are all at different redshifts. The interpretation of the result is not straightforward for the various options for the scaling relation of s .

To infer the best estimates for σ_* , and s_* of the bright sample one has to perform a maximum likelihood analysis in which the redshift of each individual galaxy is a free parameter, which has to be chosen such that it maximizes the likelihood. This approach is computationally not feasible, and we use another approach to obtain estimates for σ_* and s_* .

We use the same method that was used for the galaxies with redshifts, but instead we create mock redshift catalogs. The redshift distribution of the galaxies in the ‘bright’ sample has been measured by the CNOC2 survey. The redshifts of the galaxies in the mock catalogs are drawn randomly for the CNOC2 survey based on the apparent R magnitude of the galaxies in the ‘bright’ sample. We take the incompleteness of the survey into account when the redshifts are drawn from the survey. This mock redshift catalog allows us to determine the best estimates for σ_* and s_* , based on a maximum likelihood analysis of the observed distortion field. We repeat this procedure 25 times, and use the average χ^2 surface. The best estimates for σ_* and s_* for the three different scaling relations for s are listed in Table 5b.

We verified that this procedure yields an unbiased estimate, by simulating the data and applying the procedure described above. We used the derived values of σ_* and s_* (see Table 5b) as input values for the simulations. These simulations also allow us to estimate the scatter in the measurements. Compared to the situation where the redshift of each lens is known, the lack of redshifts increases the uncertainty in s_* by $\sim 50\%$. The uncertainty in σ_* is increased by 30%. For instance, adopting $s \propto \sigma^2$, the uncertainty in-

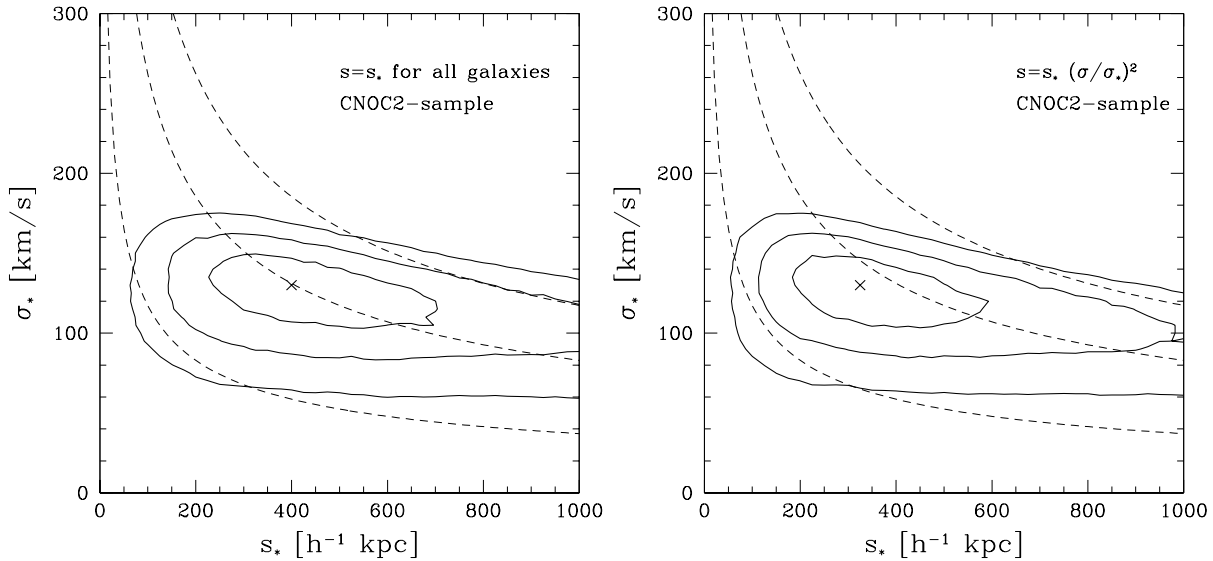


Figure 6. Likelihood contours for the velocity dispersion σ_* of an $L_B^*(z=0) = 5.6 \times 10^9 h^{-2} L_{B\odot}$ galaxy, and its truncation radius s_* . The contours indicate 68.3%, 95.4%, and 99.7% confidence limits on two parameters jointly. The cross indicates the best parameters. We use $\sigma \propto L_B^{1/4}$, and two different scaling relations for s . The dashed lines give models with a total mass of 1, 5, $10 \times 10^{12} h^{-1} M_\odot$. (a) The truncation radius s is the same for all galaxies. (b) The results when $s \propto \sigma^2$, which corresponds to the case where all galaxy have the same total mass-to-light ratio.

creases by $\sim 45 h^{-1}$ kpc and the uncertainty in σ_* increases by ~ 3 km/s.

Comparison of the results presented in Table 5b with the results obtained for the ‘CNOC2’ sample (Table 5a) shows that the estimates for σ_* and s_* are smaller, but consistent with one another. For the case that $s \propto \sigma^2$ the ‘bright’ sample yields $\sigma_* = 111 \pm 15$ km/s and $s_* = 220_{-100}^{+133} h^{-1}$ kpc, compared to $\sigma_* = 126_{-16}^{+15}$ km/s and $s_* = 313_{-81}^{+136} h^{-1}$ kpc for the ‘CNOC2’ sample. The agreement with the results from the direct averaging method is good.

The analysis of the ‘bright’ sample has ignored any available redshift information. To make optimal use of the available information, we redo the analysis as follows. For the galaxies with redshifts we use the observed values, but for the remaining galaxies we draw redshifts and luminosities from the CNOC2 survey randomly (as was done previously for all galaxies in the ‘bright’ sample). As before, we create mock catalogs which are analysed. This procedure improves the accuracy in the estimates of σ_* and s_* . The results are presented in Table 5c. Simulations show that the lack of redshifts for all galaxies with $19.5 < R < 21$ from CNOC2 increases the uncertainty in σ_* by 18% and the uncertainty in s_* by 10%, compared to the situation where full redshift information is available.

5.4 Effect of galaxy groups

It is well known that galaxies cluster, and most of the galaxies reside in groups of galaxies. If the matter in galaxy groups is associated with the halos of the group members (i.e. these halos are indistinguishable from the halos of isolated galaxies) the analysis presented above gives a fair estimate of the sizes of galaxy halos. However, if a significant fraction of

the dark matter in galaxy groups is distributed in a common group halo, the interpretation of the results becomes difficult.

Fischer et al. (2000) argued that galaxy groups complicate the interpretation of the galaxy-galaxy lensing signal. They measured the lensing signal out to large projected distances, and find that the distortion does not vanish at large radii, which is caused by large scale clustering (the angular correlation function declines relatively slowly).

Compared to Fischer et al. (2000) we have the advantage that a number of galaxy groups have been identified in the CNOC2 fields (Carlberg et al. 2001). The weak lensing signal of these groups was studied by Hoekstra et al. (2001a). They derived a mass weighted group velocity dispersion of $\langle \sigma_{\text{group}}^2 \rangle^{1/2} = 273_{-59}^{+48}$ km/s.

We will use the groups to examine their effect on the galaxy-galaxy lensing results for the galaxies with redshifts from the CNOC2 survey. In addition to the galaxies, we include the lensing signal from group halos to our mass model. The groups are placed at their observed positions, and the groups are modeled as singular isothermal spheres. To study the effect of the groups on the galaxy-galaxy lensing results we increase the velocity dispersion of the ‘groups’ from 0 km/s (the result without groups) up to 300 km/s. For each choice of the group velocity dispersion we perform a maximum likelihood analysis and determine the best estimates for σ_* and s_* .

For $\sigma_{\text{group}} < 150$ km/s the best estimates for σ_* and s_* vary by a few percent. For larger group velocity dispersions the value for σ_* and s_* decrease slowly with increasing σ_{group} . For a group velocity dispersion of 300 km/s, the value of σ_* has dropped by $\sim 10\%$, and the value of s_* has decreased by $\sim 20\%$. We note that the minimum χ^2 has

(1)	(2)	(3)	(4)	(5)	(6)	(7)
scaling s	σ_*	s_*	s_{*}^{\min}	s_{*}^{\max}	M_{tot}^*	M_{tot}/L_B^*
	[km/s]	[h^{-1} kpc]	[h^{-1} kpc]	[h^{-1} kpc]	[$10^{12}h^{-1}M_{\odot}$]	[$hM/L_{B\odot}$]
luminosity evolution $\propto (1+z)$, $L_B^*(z=0) = 5.6 \times 10^9 h^{-2}L_{B\odot}$						
(a) galaxies with redshifts from CNOC2						
$\propto \sigma^0$	126^{+14}_{-16}	403^{+169}_{-99}	105	880	$4.7^{+1.8}_{-1.2}$	839^{+321}_{-214}
$\propto \sigma^2$	126^{+14}_{-16}	313^{+136}_{-81}	86	772	$3.6^{+1.7}_{-0.8}$	643^{+304}_{-143}
$\propto \sigma^4$	124^{+14}_{-15}	236^{+105}_{-52}	73	605	$2.6^{+1.5}_{-0.6}$	464^{+268}_{-107}
(b) 'bright' sample, no individual redshifts used						
$\propto \sigma^0$	110^{+15}_{-15}	277^{+148}_{-112}	51	623	$2.4^{+1.3}_{-0.9}$	429^{+232}_{-161}
$\propto \sigma^2$	111^{+15}_{-15}	220^{+133}_{-100}	43	531	$1.9^{+1.2}_{-0.8}$	339^{+214}_{-143}
$\propto \sigma^4$	112^{+14}_{-14}	163^{+103}_{-74}	34	407	$1.4^{+0.9}_{-0.7}$	250^{+161}_{-125}
(c) 'bright' sample, using individual redshifts when available						
$\propto \sigma^0$	110^{+12}_{-12}	337^{+130}_{-100}	86	679	$2.8^{+1.2}_{-0.8}$	500^{+214}_{-143}
$\propto \sigma^2$	111^{+12}_{-12}	260^{+124}_{-73}	80	556	$2.2^{+1.2}_{-0.7}$	393^{+214}_{-125}
$\propto \sigma^4$	113^{+12}_{-12}	195^{+92}_{-63}	68	432	$1.6^{+1.0}_{-0.5}$	286^{+179}_{-89}
no luminosity evolution, $L_B^*(z=0) = 7.3 \times 10^9 h^{-2}L_{B\odot}$						
(d) galaxies with redshifts from CNOC2						
$\propto \sigma^0$	125^{+14}_{-16}	432^{+181}_{-106}	112	942	$4.9^{+1.9}_{-1.3}$	678^{+260}_{-173}
$\propto \sigma^2$	125^{+14}_{-16}	350^{+152}_{-90}	96	862	$4.0^{+1.9}_{-0.9}$	541^{+256}_{-120}
$\propto \sigma^4$	123^{+14}_{-15}	267^{+119}_{-59}	82	684	$2.9^{+1.7}_{-0.7}$	396^{+228}_{-91}
(e) 'bright' sample, no individual redshifts used						
$\propto \sigma^0$	109^{+15}_{-15}	297^{+159}_{-120}	55	727	$2.5^{+1.4}_{-0.9}$	346^{+261}_{-130}
$\propto \sigma^2$	110^{+15}_{-15}	246^{+149}_{-112}	48	593	$2.1^{+1.3}_{-0.9}$	285^{+180}_{-120}
$\propto \sigma^4$	111^{+14}_{-14}	184^{+116}_{-84}	38	460	$1.6^{+1.0}_{-0.8}$	213^{+137}_{-107}
(f) 'bright' sample, using individual redshifts when available						
$\propto \sigma^0$	109^{+12}_{-12}	361^{+139}_{-107}	92	727	$2.9^{+1.3}_{-0.8}$	404^{+173}_{-115}
$\propto \sigma^2$	110^{+12}_{-12}	290^{+139}_{-82}	89	621	$2.4^{+1.3}_{-0.8}$	331^{+180}_{-105}
$\propto \sigma^4$	112^{+12}_{-12}	221^{+104}_{-71}	77	489	$1.8^{+1.1}_{-0.6}$	244^{+153}_{-76}

Table 5. (a) Results from the maximum likelihood analysis using the galaxies with redshifts from the CNOC2 survey. (b) The results for the analysis of the ‘bright’ sample. (c) Results when we use the observed redshifts if available, and the redshift distribution if the redshift has not been measured. (d)-(f) list the results for no luminosity evolution, for which case $L_B^*(z=0) = 7.3 \times 10^9 h^{-2}L_{B\odot}$. Only the results presented in (a) and (d) are real maximum likelihood parameters. See the text for more details. The errors correspond to 68.3% confidence. (1) the scaling relation used for the truncation parameter s ; (2) estimate for σ_* ; (3) estimate for s_* ; (4) 99.7% confidence lower limit on s_* ; (5) 95% confidence upper limit on s_* ; (6) estimate for the total mass; (7) total mass-to-light ratio of an L_B^* galaxy.

increased significantly for $\sigma_{\text{group}} = 300$ km/s, compared to $\sigma_{\text{group}} = 0$ km/s.

Ideally one would like to use different halo models for the group members and the ‘isolated’ galaxies and study the difference in the best parameters for these two types of galaxies. With the current data we cannot perform such an analysis, because the number of group members is too low. However, our results are based on approximately one quarter of the full CNOC2 data set. An analysis of the full survey will improve the signal-to-noise ratio of the measurements by a factor ~ 2 , and will allow a better study of the effect of galaxy groups. Also numerical simulations can be useful to examine if, and how one can separate the contribution of the galaxy halos and the smooth group halos.

5.5 Comparison with other lensing studies

Other studies selected different samples of lenses, used different scaling relations, or made other assumptions about the luminosity evolution. Fortunately, sufficient information is available to allow for a useful, if crude, comparison. We will compare the findings of some other studies to the results from our maximum likelihood analysis.

The typical lens galaxy in the sample studied by Hudson et al. (1998) is at $z \sim 0.6$, and has $M_B = -18.5 + 5 \log h$ (for $g_0 = 0.5$). Hudson et al. (1998) derived a circular velocity of 210 ± 40 km/s. This corresponds to a galaxy with a luminosity of $L_B(z=0) \sim 3.2 \times 10^9 h^{-2}L_{B\odot}$ for our choice of cosmology and luminosity evolution. Our weak lensing analysis suggests a circular velocity of $V_c = 119 \pm 12$ km/s

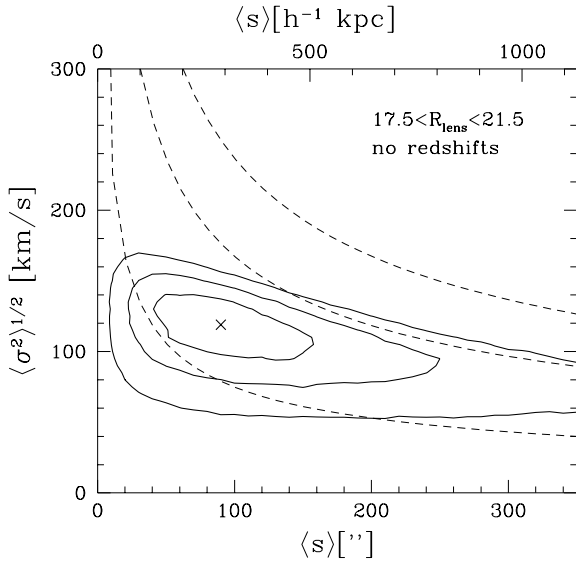


Figure 7. Likelihood contours for the velocity dispersion σ_* of an $L_B^*(z=0) = 5.6 \times 10^9 h^{-2} L_{B\odot}$ galaxy, and the average value of the truncation radius $\langle s \rangle$ as determined from the ‘bright’ sample. We have also indicated the physical scale when s is the same for all galaxies. The contours indicate 68.3%, 95.4%, and 99.7% confidence limits on two parameters jointly. The cross indicates the best parameters. The dashed lines give models with a total mass of 1, 5, $10 \times 10^{12} h^{-1} M_{\odot}$.

for such a galaxy. If we assume no luminosity evolution (as Hudson et al. (1998) did), we obtain a circular velocity of $V_c = 130 \pm 14$. The two results are inconsistent at the $\sim 2\sigma$ level. It is not clear, however, how to interpret the difference in circular velocity, as our weak lensing analysis probes a larger physical scale than Hudson et al. (1998), and the mix of galaxy types might also be different.

Fischer et al. (2000) measured the galaxy-galaxy lensing signal with much higher accuracy than Hudson et al. (1998) from SDSS data. Fischer et al. (2000) find for their sample of lenses an average mass weighted velocity dispersion of $\langle \sigma^2 \rangle^{1/2} = 145 - 195$ km/s (95% confidence). McKay et al. (2001) noted that the SDSS redshift survey showed that the lens redshifts used by Fischer et al. (2000) were overestimated by $\sim 35\%$. The correct range in line-of-sight velocity dispersion of the Fischer et al. (2000) analysis should be $\langle \sigma^2 \rangle^{1/2} \approx 105 - 145$ km/s.

Most of the signal comes from galaxies with luminosities around $L_{g'} = 8.7 \times 10^9 h^{-2} L_{g'\odot}$ (P. Fischer, private communication). If we use an average $B - V = 0.55$ and the transformations from Fukugita et al. (1996), we find that the adopted B band luminosity of our L_B^* galaxy corresponds to a g' band luminosity of $L_{g'} = 6 \times 10^9 h^{-2} L_{g'\odot}$. Our lensing analysis implies a velocity dispersion of $\sigma = 122_{-12}^{+13}$ km/s (68.3% confidence) for a galaxy with $L_{g'} = 8.7 \times 10^9 h^{-2} L_{g'\odot}$, which agrees well with the Fischer et al. (2000) result.

McKay et al. (2001) used a sample of galaxies with spectroscopic redshifts from the SDSS. Their sample of lenses is comparable in size to the one used by Fischer et al. (2000). Using the complete sample, McKay et al. (2001) find a ve-

locity dispersion $\sigma = 100 - 130$ km/s (95% confidence) with a best fit value of $\sigma = 113$ km/s for a galaxy with $L_{g'\odot} \sim 9 \times 10^9 h^{-2} L_{g'\odot}$. For such a galaxy, our lensing analysis yields $\sigma = 122_{-12}^{+13}$ km/s (68.3% confidence), in excellent agreement with McKay et al. (2001).

Fischer et al. (2000) and McKay et al. (2001) also attempted to constrain the sizes of galaxy halos. Both studies indicate that the galaxy halos are large. Unfortunately it is not clear what the correct value for the Fischer et al. (2000) result is. McKay et al. (2001) used the same approach as Fischer et al. (2000) and find a lower limit of $s^{\text{min}} = 230 h^{-1}$ kpc (95% confidence). McKay et al. (2001) do not use any scaling for s (they assume all halos are the same) and their results should be compared to our results for constant s for all galaxies. We obtain an estimate of $s = s_* = 337_{-100}^{+130} h^{-1}$ kpc, which is in good agreement with McKay et al. (2001).

Interestingly, McKay et al. (2001) find that the mass within an aperture of radius $260 h^{-1}$ kpc scales proportional to the luminosity of the lens. This appears to be in contradiction with the naive expectation from the Tully-Fischer or Faber-Jackson relation, which suggests $M \propto \sqrt{L}$. However, the latter is no longer true for truncated halos. As discussed in Section 5.3, the relation between the mass and luminosity on large scales depends on the adopted scaling relation for s (at large radii $M \propto \sigma^2 s$). For instance, $s \propto \sigma^2$ results in $M \propto L$ at radii (much) larger than s .

Hence, the results presented by McKay et al. (2001) suggest that the truncation is smaller than $260 h^{-1}$ kpc. This is likely to be the case for the faint lenses, but the brighter lenses are expected to have larger halos. However, luminous galaxies are clustered more strongly (e.g., Norberg et al. 2002) and the contribution from neighboring galaxies could bias the lensing signal somewhat high, although the effect is expected to be small (McKay et al. 2001).

Recently, Yang et al. (2002) used numerical simulations to study the results presented by McKay et al. (2001). The galaxies in the simulations obey the Tully-Fischer or Faber-Jackson relation. Yang et al. (2002) find that the aperture mass within $260 h^{-1}$ kpc is proportional to the luminosity of the lens. The results from Yang et al. (2002), however, suggest that the linear relation found by McKay et al. (2001) is a coincidence, because they find that the halo mass scales $\propto L^{1.5}$ (which corresponds to $s \propto \sigma^4$). The mass with an aperture of radius $260 h^{-1}$ kpc results in a linear relation, whereas other apertures would yield different results.

Finally we note that the results presented here are in good agreement with preliminary results from an analysis of R band imaging data from the Red-Sequence Cluster Survey (RCS). Hoekstra, Yee, & Gladders (2001d) use lenses with $19.5 < R < 21$. Their results imply $\sigma_* = 102 \pm 4$ km/s and $s_* = 198_{-19}^{+25} h^{-1}$ kpc for an $L_B^*(z=0) = 5.6 \times 10^9 h^{-2} L_{B\odot}$ galaxy (adopting $s \propto \sigma^2$), which is in good agreement with our results.

5.6 Comparison with Tully-Fisher relation

Comparison of the luminosity and the rotation velocity of gas in spiral galaxies has shown that there exists a tight relation between these two observables: the Tully-Fisher (TF) relation. Note, however, that weak lensing probes the mass on a much larger scale than the rotation curve. For example,

if the rotation curve is slowly declining, the lensing result will be lower (compared to the flat rotation curve). Furthermore, the sample of lenses used here is different from the sample of spiral galaxies used for the TF relation. Ideally one would like to select a sample of spiral galaxies for this comparison, but this is outside the scope of this paper. Nevertheless, it is interesting to compare our lensing result to a local determination of the TF relation.

One of the most recent determinations of the TF relation was presented by Verheijen (2001), who studied a large sample of galaxies in the Ursa Major cluster of galaxies. The sample has the advantage that the galaxies are at a distance of 18.6 Mpc (Tully & Pierce 2000). This allowed Verheijen (2001) to study the scatter in the TF relation.

Verheijen (2001) has measured V_{flat} , the rotation velocity of the ‘flat’ part of the rotation curve, which is representative for the mass of the galaxy. As is customary in TF studies, Verheijen (2001) used extinction corrected luminosities. The luminosities used in our lensing analyses, however, have not been corrected for inclination and extinction. To allow a direct comparison with the weak lensing results, we use the uncorrected magnitudes from Tully et al. (1996). The resulting TF relation is presented in Figure 8 (open dots with error bars).

The hatched region indicates the 1σ interval around the TF relation, based on the scatter in the observations. In the comparison we use the circular velocity corresponding to the value of σ_* (assuming $s \propto \sigma^2$) listed in Table 5c. We assume that $V_{\text{flat}} = \sqrt{2}\sigma$. The result is indicated by the large black dot. The comparison depends on the value of the Hubble parameter, because the inferred luminosities of the lenses in our analysis depend on h , whereas the absolute magnitudes of the galaxies from Verheijen (2001) are based on the adopted distance to the Ursa Major cluster (and therefore do not depend on the Hubble parameter). For the comparison presented in Figure 8 we adopted a value of $H_0 = 70$ km/s/Mpc. Although one cannot make a direct comparison between the weak lensing results and the TF relation (for reasons mentioned above) it is comforting that the results are rather similar.

6 MASS-TO-LIGHT RATIO AND Ω_M

A useful method to estimate the matter density of the universe was proposed by Oort (1958): Ω_m is the product of the average mass-to-light ratio of the universe, and its luminosity density. Carlberg et al. (1997) measured the mass-to-light ratios of rich clusters of galaxies, and inferred $\Omega_m = 0.19 \pm 0.06$. The galaxy properties of rich clusters are different from those of the field, and a large correction is needed to relate the cluster mass-to-light ratio to that of the field. Smaller corrections are required when galaxy groups are used. Hoekstra et al. (2001a) derived $\Omega_m = 0.19 \pm 0.1$ from their weak lensing analysis of 50 groups. Bahcall & Comerford (2002) found $\Omega_m = 0.17 \pm 0.05$ from a combination of clusters and groups.

A measurement of the average mass-to-light ratio of field galaxies has the advantage that no additional corrections for the difference in stellar populations are required. An estimate for the average mass-to-light ratio of the field, i.e., the universe as a whole, can be obtained from the re-

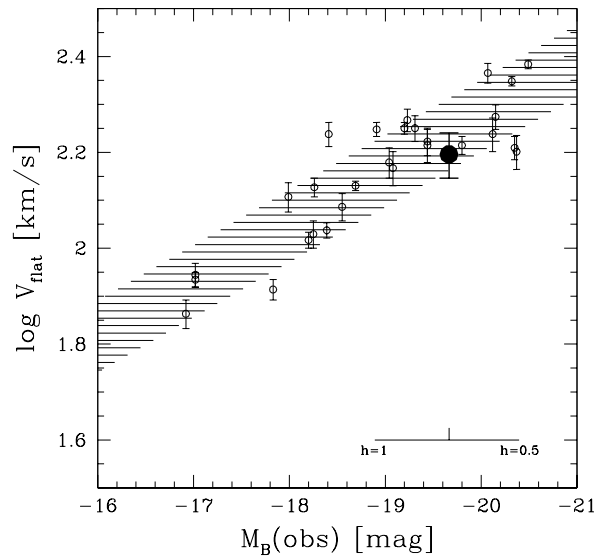


Figure 8. Plot of rotation velocity of the ‘flat’ part of the rotation curve V_{flat} versus the absolute B-band magnitude (uncorrected for inclination and extinction). The open dots with error bars indicate the measurements of Verheijen (2001), using the (uncorrected) magnitudes from Tully et al. (1996). The hatched region indicates the 1σ interval around the derived TF relation. In the comparison we use the circular velocity corresponding to the value of σ_* (assuming $s \propto \sigma^2$) listed in Table 5c. The result is indicated by the large black dot. The comparison depends on the value of the Hubble parameter, because the inferred luminosities of the lenses in our analysis depend on h , whereas the absolute magnitudes of the galaxies from Verheijen (2001) are based on the adopted distance to the Ursa Major cluster, and therefore do not depend on the value of the Hubble parameter. The inferred luminosities of the galaxies studied in the weak lensing analysis do depend on H_0 , and for the comparison we take a value of $H_0 = 70$ km/s/Mpc. We have also indicated how the weak lensing result would change with h . The weak lensing result is in good agreement with the observed TF relation. We note that weak lensing probes the mass on a much larger scale than the rotation curve, and one therefore might expect only a qualitative agreement. Furthermore, the sample of lenses is rather different from the sample of spiral galaxies used for the TF relation.

sults of our maximum likelihood analysis. The inferred total mass-to-light ratio, however, depends on the assumed scaling relation for the truncation parameter s (as is apparent from column 7 in Table 5).

Lin et al. (1999) have determined the luminosity function of field galaxies from the CNOC2 survey, and we use their results to estimate the average mass-to-light ratio of the field. The results are listed in Table 6 (column 4). When $s \propto \sigma^2$, the average mass-to-light ratio equals that of an L_B^* galaxy. In the case that all halos have the same value for s , we already found that the resulting mass-to-light ratio of an L_* galaxy is high, but in addition, fainter galaxies have even higher mass-to-light ratios. This results in a very high field mass-to-light ratio. On the other hand, if $s \propto \sigma^4$, faint galaxies have low mass-to-light ratios, and the field mass-to-light ratio is somewhat lower than that of an L_B^* galaxy.

To estimate the luminosity density of the universe we use the results from Lin et al. (1999), which are also based on the CNOC2 survey. We convolve the redshift distri-

(1)	(2)	(3)	(4)	(5)	(6)
scaling s	scaling M/L_B	$M_{\text{tot}}/L_B^*(z=0)$ [$hM/L_{B\odot}$]	$\langle M/L_B \rangle (z=0)$ [$hM/L_{B\odot}$]	$\langle M/L_B \rangle (z=0.34)$ [$hM/L_{B\odot}$]	Ω_m
$\propto \sigma^0$	$\propto 1/\sqrt{L_B}$	500^{+214}_{-143}	850^{+364}_{-243}	634^{+272}_{-181}	$0.69^{+0.30}_{-0.20}$
$\propto \sigma^2$	constant	393^{+214}_{-125}	393^{+214}_{-125}	293^{+160}_{-93}	$0.32^{+0.17}_{-0.10}$
$\propto \sigma^4$	$\propto \sqrt{L_B}$	286^{+179}_{-89}	240^{+150}_{-75}	168^{+112}_{-56}	$0.18^{+0.12}_{-0.06}$

Table 6. Estimates for the average field mass-to-light ratio for different scaling relations of the truncation parameter s . The errors correspond to 68.3% confidence. (1) the scaling relation used for the truncation parameter s ; (2) the dependence of the total mass-to-light ratio on the luminosity; (3) total mass-to-light ratio of an L_B^* galaxy; (4) average field mass-to-light ratio at $z=0$; (5) average field mass-to-light ratio at the average redshift of the sample of galaxies ($z=0.34$); (6) estimate for the matter density of the universe Ω_m .

bution of the galaxies with the redshift dependent luminosity density from Lin et al. (1999), which yields $j = (3.0 \pm 0.6) \times 10^8 h L_{B\odot} \text{Mpc}^{-3}$. We use this result, and our estimates for the average field mass-to-light ratio at $z=0.34$ to derive the corresponding values of Ω_m , which are listed in column 6 of Table 6.

With the current data, the statistical error in the value of Ω_m is large. In addition, the uncertainty in the scaling relation of s limits the determination of Ω_m through this technique. We also assumed that all matter in the universe is associated with the galaxy dark matter halos. The lensing signal is not changed by adding a sheet of constant surface density (Gorenstein, Shapiro, & Falco 1988). Thus a uniformly distributed form of dark matter cannot be detected in our analysis. Consequently, our estimate for Ω_m should be interpreted as a lower limit. Another approach is to use independent measurements of Ω_m (e.g., from CMB or cosmic shear studies) to constrain the scaling relation for s .

7 CONCLUSIONS

We observed two blank fields of approximately 30 by 23 arcminutes using the William Herschel Telescope. The fields were studied as part of the Canadian Network for Observational Cosmology Field Galaxy Redshift Survey (CNOC2) (e.g., Yee et al. 2000; Carlberg et al. 2001), and spectroscopic redshifts are available for 1125 galaxies in the two fields. Earlier results on groups of galaxies, based on these data, were presented by Hoekstra et al. (2000a).

We have measured the lensing signal caused by large scale structure. We observed signal is low, and consistent with more accurate measurements from much larger surveys (e.g., Bacon et al. 2002; Hoekstra et al. 2002a,b; Refregier et al. 2002; van Waerbeke et al. 2002).

We examined the effect of an imperfect correction for PSF anisotropy, and find the correction used here has worked well: it gives the smallest cosmic shear signal. In addition we find that the uncertainty in the correction has a negligible effect on the galaxy-galaxy lensing results.

We have studied the ensemble averaged tangential distortion (galaxy-mass correlation function) around three subsamples of lenses. In all three cases a clear lensing signal is detected. We relate the lensing signal to an estimate of the velocity dispersion of an L_B^* galaxy, and find that the results for the three samples agree well with each other. For the sample of galaxies with redshifts from the CNOC2 survey we derive $\sigma_* = 130^{+15}_{-17}$ km/s (or $V_c^* = 184^{+22}_{-25}$ km/s).

Note, however, that this measurement is slightly biased, because of the clustering of the lenses.

To study the properties of the dark matter halos surrounding the lens galaxies, we used a maximum likelihood analysis. This technique allowed us to derive constraints on both the velocity dispersion and the extent of the dark matter halos (it naturally accounts for the clustering of the lenses). The value of the truncation parameter s depends strongly on the assumed scaling relation, but the velocity dispersion is well constrained. Galaxy groups can complicate the interpretation of the truncation parameter s . We examined how galaxy groups affect our results, and we find that their effect is relatively small. Our data are not sufficient for a detailed study, but the full CNOC2 data set can be useful to this end, as well as studies of numerical simulations.

Under the assumption that all galaxies have the same total mass-to-light ratio, we find a value of $\sigma_* = 111 \pm 12$ km/s (68% confidence, marginalised over the truncation parameter s) for the velocity dispersion of an L_B^* galaxy. For the truncation parameter we obtain $s_* = 260^{+124}_{-73} h^{-1}$ kpc (68% confidence, marginalised over σ_*), with a 99.7% confidence lower limit of $80 h^{-1}$ kpc, and a 95% confidence upper limit of $556 h^{-1}$ kpc. For this model we find that the average field mass-to-light ratio at $z=0$ is $393^{+214}_{-124} M_\odot/L_{B\odot}$, comparable to what is found for rich clusters of galaxies (Carlberg et al. 1997) and galaxy groups (Hoekstra et al. 2001a).

The field mass-to-light ratio provides an estimate of Ω_m , the matter density of the universe. The results from the weak lensing analysis provide a lower limit on Ω_m , because lensing cannot detect dark matter that is distributed uniformly through the universe. Unfortunately, our estimate of the field mass-to-light ratio, and consequently the derived value of Ω_m , depends strongly on the assumed scaling of s .

The results presented here demonstrate that weak lensing is a powerful tool to study the dark matter halos of field galaxies, as it can probe the mass distribution out to large projected distances. In this paper we have used approximately one quarter of the CNOC2 survey. An analysis of the full survey will improve the accuracy of the results by a factor ~ 2 . Furthermore, many large imaging surveys are currently underway. First results from the Red-Sequence Cluster Survey (RCS) indicate that these surveys can provide accurate constraints on the dark matter halos of field galaxies (e.g., Hoekstra et al. 2002d).

ACKNOWLEDGEMENTS

It is a pleasure to thank the members of the Canadian Network for Observational Cosmology without whom this project would never have been possible. We thank Jocelyn Bézecourt for his help to obtain part of the imaging data. The WHT observations for this project have been supported financially by the European Commission through the TMR program 'Access to large-scale facilities', awarded to the Instituto de Astrofísica de Canarias. HH acknowledges support from the Leidsch Kerkhoven-Bosscha Fonds and the University of Toronto.

REFERENCES

- Bacon, D., Refregier, A., & Ellis, R.S. 2000, MNRAS, 325, 1065
 Bacon, D., Massey, R., Refregier, A., & Ellis, R. 2002, MNRAS, submitted, astro-ph/0203134
 Bahcall, N.A., & Comerford, J.M. 2002, ApJ, 565, 5
 Bernardeau, F., van Waerbeke, L., Mellier, Y. 1997, A&A, 322, 1
 Bonnet, H., Mellier, Y., & Fort, B. 1994, ApJ, 427, L83
 Blandford, R.D., Saust, A.B., Brainerd, T.G., & Villumsen, J.V. 1991, MNRAS, 251, 600
 Brainerd, T.G., Blandford, R.D., & Smail, I. 1996, ApJ, 466, 623
 Carlberg, R.G., Yee, H.C., & Ellingson 1997, ApJ, 478, 462
 Carlberg, R.G., Yee, H. K. C., Morris, S. L., Lin, H., Hall, P. B., Patton, D. R., Sawicki, M., & Shepherd, C. W. 2001, ApJ, 552, 427
 Dell'Antonio, I.P., & Tyson, J.A. 1996, ApJ, 473, L17
 Erben, T., van Waerbeke, L., Mellier, Y., Schneider, P., Cuillandre, J.-C., Castander, F.J., Dantel-Fort, M. 2000, A&A, 355, 23
 Fahlman, G., Kaiser, N., Squires, G., & Woods, D. 1994, ApJ, 437, 56
 Fernández-Soto, A., Lanzetta, K.M., & Yahil, A. 1999, ApJ, 513, 34
 Fischer, P., et al. 2000, AJ, 120, 1198
 Fukugita, M., Ichikawa, T., Gunn, J.E., Doi, M., Shimasaku, K., & Schneider, D.P. 1996, AJ, 111, 1748
 Gorenstein, M.V., Shapiro, I.I., & Falco, E.E. 1988, ApJ, 327, 693
 Griffiths, R.E., Casertano, S., Im, M., & Ratnatunga, K.U. 1996, MNRAS, 282, 1159
 Hoekstra, H., Franx, M., Kuijken, K., & Squires, G. 1998, ApJ, 504, 636
 Hoekstra, H., Franx, M., Kuijken, K. 2000a, ApJ, 532, 88
 Hoekstra, H. 2001, A&A, 370, 743
 Hoekstra, H., et al. 2001a, ApJ, 548, L5
 Hoekstra, H., Yee, H.K.C., & Gladders, M.D. 2001, 558, L11
 Hoekstra, H., Yee, H.K.C., Gladders, M.D., Barrientos, L.F., Hall, P.B., & Infante, L. 2002a, ApJ, 572, 55
 Hoekstra, H., Yee, H.K.C., & Gladders, M.D. 2002b, ApJ, 577, 604
 Hoekstra, H., van Waerbeke, L., Gladders, M.D., Mellier, Y., & Yee, H.K.C. 2002c, ApJ, 577, 595
 Hoekstra, H., Yee, H.K.C., & Gladders, M.D. 2002d, NewAR, 46, 767
 Hudson, M.J., Gwyn, S.D.J., Dahle, H., & Kaiser, N. 1998, ApJ, 503, 531
 Jain, B., & Seljak, U. 1997, ApJ, 484, 560
 Kaiser, N. 1992, ApJ, 388, 272
 Kaiser, N., & Squires, G. 1993, ApJ, 404, 441
 Kaiser, N., Squires, G., & Broadhurst, T. 1995, ApJ, 449, 460
 Kaiser, N., Wilson, G., & Luppino, G.A. 2000, ApJL, submitted, astro-ph/0003338
 Landolt, A.U. 1992, AJ, 104, 340
 Lin, H., Yee, H.K.C., Carlberg, R.G., Morris, S.L., Sawicki, M., Patton, D.R., Wirth, G., & Shepherd, C.W. 1999, ApJ, 518, 533
 Luppino, G.A., Kaiser, N. 1997, ApJ, 475, 20
 Madgwick, D.S., et al. 2002, MNRAS, 333, 133
 McKay, T.A., et al. 2001, ApJ, submitted, astro-ph/0108013
 Mellier, Y. 1999, ARA&A, 37, 127
 Norberg, P., et al. 2002, MNRAS, 332, 827
 Oort, J.H. 1958, in La Structure et L'évolution de L'Univers, Onzième Conseil de Physique, ed. R. Stoops (Solvay: Bruxelles), 163
 Press, W.H., Teukolsky, S.A., Vetterling, W.T. & Flannery, B.P. 1992, Numerical Recipes in C, Cambridge University Press
 Refregier, A., Rhodes, J., & Groth, E.J. 2002, ApJ, 572, L131
 Schneider, P., & Rix, H.-W. 1997, ApJ, 474, 25
 Schneider, P., van Waerbeke, L., Jain, B., & Kruse, G. 1998, MNRAS, 296, 873
 Smith, D.R., Bernstein, G.M., Fischer, P., & Jarvis, M. 2001, ApJ, 551, 643
 Squires, G. & Kaiser, N. 1996, ApJ, 473, 65
 Squires, G., Kaiser, N., Babul, A., Fahlman, G., Woods, D., Neumann, D.M., & Boehringer, H. 1996, ApJ, 461, 572
 Tully, R.B., Verheijen, M.A.W., Pierce, M.J., Huang, J.-S., & Wainscoat, R.J. 1996, AJ, 112, 2471
 Tully, R.B., & Pierce, M.J. 2000, ApJ, 533, 744
 Tyson, J.A., Valdes, F., Jarvis, J.F., & Mills, A.P., Jr. 1984ApJ, 281, L59
 Tyson, J.A., Wenk, R.A., & Valdes, F. 1990, ApJ, 349, 1
 van Albada, T. S., & Sancisi, R. 1986, RSLPT, 320, 447
 van Dokkum, P.G., & Franx, M. 1996, MNRAS, 281, 985
 van Waerbeke, L., et al. 2000, A&A, 358, 30
 van Waerbeke, L., et al. 2001, A&A, 374, 757
 van Waerbeke, L., Mellier, Y., Pello, R., Pen, U.-L., McCracken, H.J., Jain, B. 2002, A&A, 393, 369
 Verheijen, M.A.W. 2001, ApJ, 563, 694
 White, M., van Waerbeke, L., & Mackey, J. 2002, ApJ, 575, 640
 Wilson, G., Kaiser, N., Luppino, G.A. 2001, ApJ, 556, 601
 Wittman, D.M., Tyson, J.A., Kirkman, D., Dell'Antonio, I., & Bernstein, G. 2000, Nature, 405, 143
 Wittman, D., Tyson, J.A., Margoniner, V.E., Cohen, J.G., & Dell'Antonio, I. P. 2001, ApJ, 557, 89
 Yang, X.-H., Mo, H.J., Kauffmann, G., & Chu, Y.-Q. 2002, MNRAS, submitted, astro-ph/0205546
 Yee, H.K.C., et al. 2000, ApJS, 129, 475
 Zaritsky, D., & White, S.D.M. 1994, ApJ, 435, 599